Supporting Information

High-performance bifacial semitransparent organic photovoltaics featuring a decently transparent TeO_2/Ag electrode

Xin Liu, Yunsen Zhao, Jiangsheng Yu*, and Rihong Zhu*

MIIT Key Laboratory of Advanced Solid Laser, School of Electronic and Optical Engineering, Nanjing University of Science and Technology, Nanjing 210094, PR China

* Corresponding authors.

E-mail: yjs@njust.edu.cn, zhurihong@njust.edu.cn

SCLC Mobility Measurements

Electron-only devices with the configuration of ITO/ZnO/active layer/PDINN/Ag and hole-only devices with the configuration of ITO/PEDOT:PSS/active layer/MoO_3/Ag were used to evaluate charge mobilities by SCLC model. The charge mobilities were determined by fitting the dark current according to the following equation:

$$J = \frac{9}{8}\varepsilon_r\varepsilon_0\mu\frac{V^2}{L^3}$$

Where J is the dark current density (mA cm^{-2}), ε_r is the permittivity of free space, ε_0 is the dielectric constant of the blend material, V is the effective voltage and L is the thickness of the active layer.

Color coordinates (x, y)

Color coordinates (x, y) for evaluating ST-OPVs. The CIE 1931 xyz chromaticity diagram, as designed for human eye perception, can be used to evaluate the color property of illuminants. The color coordinate (x, y, z) of ST-OPVs can be calculated according to the corresponding transmitted light. The sum of color coordinate (x, y, z) is equal to 1, so that the color coordinates can be simplified to two-dimensional coordinates (x, y). Standard daylight illuminant AM 1.5G (0.3202, 0.3324) and D65 (0.3128, 0.3290) are commonly chosen as reference light sources for evaluating the color property of ST-OPVs.[1,2] The color coordinates of neutral color ST-OPVs are close to (0.3333, 0.3333) or that of illuminant AM 1.5G and D65, which are generally preferred for solar widow application.

Correlative color temperature (CCT) and color rendering index (CRI)

When the spectral components of light source are the same as the spectral components emitted by the black body at a certain absolute temperature, the temperature is defined as correlative color temperature (CCT) of the light source. The CCT is the temperature of a black body radiator having the closest chromaticity as the illuminant. In the CIE 1931 chromaticity diagram, the straight black lines are constant temperature lines, and the curved black line that crosses with constant temperature lines is defined as black body locus or Planck locus. The color rendering index (CRI) is another important parameter to evaluate the performance of the ST-OPVs. The value of CRI can be obtained by comparing the color rendering of a reference light source to that of a test light source, which can quantitatively exhibit the ability of a test light source to reveal the color of an object compared with a reference or natural light source. The CRI value is defined as the value from 0 to 100. The higher CRI, the better color rendering ability and the higher neutral color degree. For the ST-OPVs, the CRI can be evaluated according to the matching degree between the transmitted light from the devices and the illumination light.

Principle of anti-reflective film

For a single-layer reflective film, when a light beam is incident, it is reflected several times within the film and a series of beams are emitted parallel to each other on both surfaces (**Figure** S3a).

Assuming that the thickness of the film is h, the refractive index is n_1, the refractive index of the substrate is n_2, and light is incident on the film from a medium with refractive index n_0.

Using a similar treatment of parallel flat plate multi-beam interference, the reflection coefficient at a single level can be obtained as follows:

$$r = \frac{r_1 + r_2 e^{i\varphi}}{1 + r_1 r_2 e^{i\varphi}}$$

The formula r_1 is the reflection coefficient on the upper surface of the film, r_2 is the reflection coefficient on the lower surface of the film, φ is the phase difference between two adjacent outgoing beams,

$$\varphi = \frac{4\pi}{\lambda} n_1 h cos\theta_1$$

The reflectivity R of a single-layer film is

$$R = \frac{r_1^2 + r_1^2 + 2r_1 r_2 cos\varphi}{1 + r_1^2 r_2^2 + 2r_1 r_2 cos\varphi}$$

When the beam is positively incident on the film, the reflection coefficients of the two surfaces are

$$r_1 = \frac{n_0 - n_1}{n_0 + n_1}$$
$$r_2 = \frac{n_1 - n_2}{n_1 + n_2}$$

Substituting this into the above equation, the reflectivity formula of single-layer film at positive incidence can be obtained,

$$R = \frac{(n_0 - n_2)^2 cos^2\frac{\varphi}{2} + (\frac{n_0 n_2}{n_1} - n_1)^2 sin^2\frac{\varphi}{2}}{(n_0 + n_2)^2 cos^2\frac{\varphi}{2} + (\frac{n_0 n_2}{n_1} + n_1)^2 sin^2\frac{\varphi}{2}}$$

Thus for a given substrate and dielectric film, $n_1$and n_2 are constants, and R can be obtained from the above equation as φ or $n_1 h$ varies.

For multi-layer reflective films, the equivalent interface and matrix methods are usually used to calculate the optical properties of multi-layer film systems. A double-layer reflective reduction film by the equivalent interface method is shown in **Figure** S3b. The first consideration is the reflection coefficient and phase difference of a monolayer system consisting of a second film adjacent to the substrate.

$$\bar{r} = \frac{r_2 + r_3 e^{i\varphi_2}}{1 + r_2 r_3 e^{i\varphi_2}}$$

$$\varphi_2 = \frac{4\pi}{\lambda} n_2 h_2 cos\theta_2$$

Further, we consider the above single-layer film system as a "new substrate" with a refractive index of n_I (the equivalent refractive index).

The reflectance and phase difference of a monolayer system consisting of the first film and "new substrate" are

$$r = \frac{r_1 + \bar{r} e^{i\varphi_1}}{1 + r_1 \bar{r} e^{i\varphi_2}}$$

$$\varphi_1 = \frac{4\pi}{\lambda} n_1 h_1 cos\theta_1$$

The final reflectance of the double film system can be obtained as follows.

$$R = \frac{c^2 + d^2}{a^2 + b^2}$$

$$a = (1 + r_1 r_2 + r_2 r_3 + r_3 r_1) cos\frac{\varphi_1}{2} cos\frac{\varphi_2}{2} - (1 - r_1 r_2 + r_2 r_3 - r_3 r_1) sin\frac{\varphi_1}{2} sin\frac{\varphi_2}{2}$$

$$b = (1 - r_1 r_2 - r_2 r_3 + r_3 r_1) sin\frac{\varphi_1}{2} cos\frac{\varphi_2}{2} + (1 + r_1 r_2 - r_2 r_3 - r_3 r_1) cos\frac{\varphi_1}{2} sin\frac{\varphi_2}{2}$$

$$c = (r_1 + r_2 + r_3 + r_3 r_1 r_2) cos\frac{\varphi_1}{2} cos\frac{\varphi_2}{2} - (r_1 - r_2 + r_3 - r_3 r_1 r_2) sin\frac{\varphi_1}{2} sin\frac{\varphi_2}{2}$$

$$d = (r_1 - r_2 - r_3 + r_3 r_1 r_2) sin\frac{\varphi_1}{2} cos\frac{\varphi_2}{2} + (r_1 + r_2 - r_3 - r_3 r_1 r_2) cos\frac{\varphi_1}{2} sin\frac{\varphi_2}{2}$$

For multi-layer antireflective film (**Figure** S3c), in principle, the above-mentioned equivalent interface concept is used to calculate the reflectance.

Starting from layer k adjacent to the substrate, an equivalent interface is formed with a reflection coefficient and phase difference of

$$\bar{r}_k = \frac{r_k + r_{k+1}e^{i\varphi_k}}{1 + r_k r_{k+1}e^{i\varphi_k}}$$

$$\varphi_k = \frac{4\pi}{\lambda} n_k h_k cos\theta_k$$

A further layer k-1 is added to form a new equivalent interface with a reflection coefficient and phase difference of

$$\bar{r}_k = \frac{r_{k-1} + r_k e^{i\varphi_{k-1}}}{1 + r_{k-1} r_k e^{i\varphi_{k-1}}}$$

$$\varphi_{k-1} = \frac{4\pi}{\lambda} n_{k-1} h_{k-1} cos\theta_{k-1}$$

Repeating this calculation process until the first layer of film adjacent to air, the final reflection coefficient and reflectance of the entire film system can be obtained.

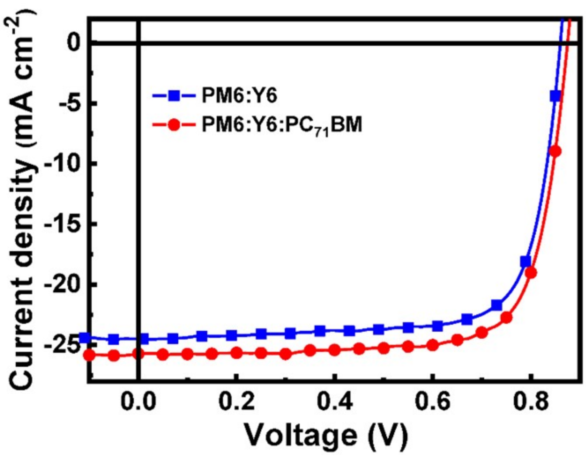

Figure S1. *J-V* curve of opaque OPVs using PM6:Y6 and PM6:Y6:$PC_{71}BM$ as active layers.

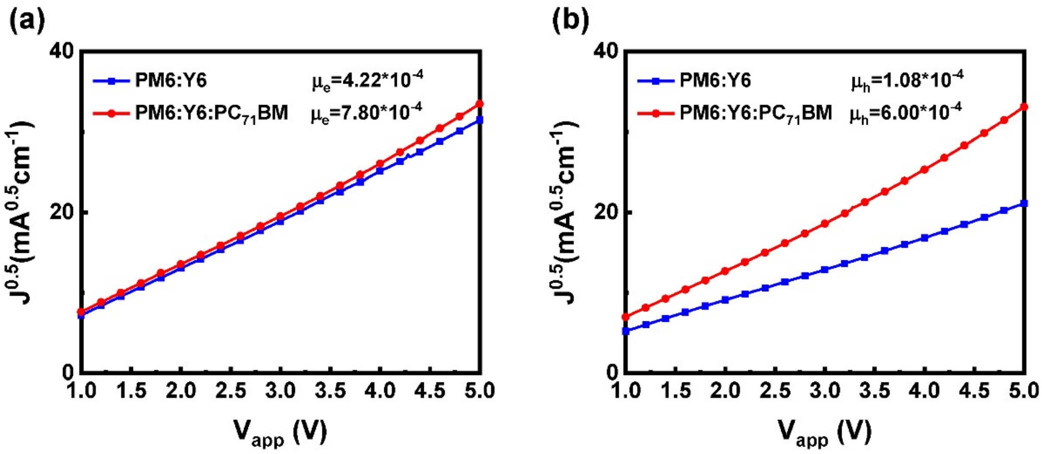

Figure.S2. The $J^{0.5}$-V curves of (a) electron-only and (b) hole-only devices.

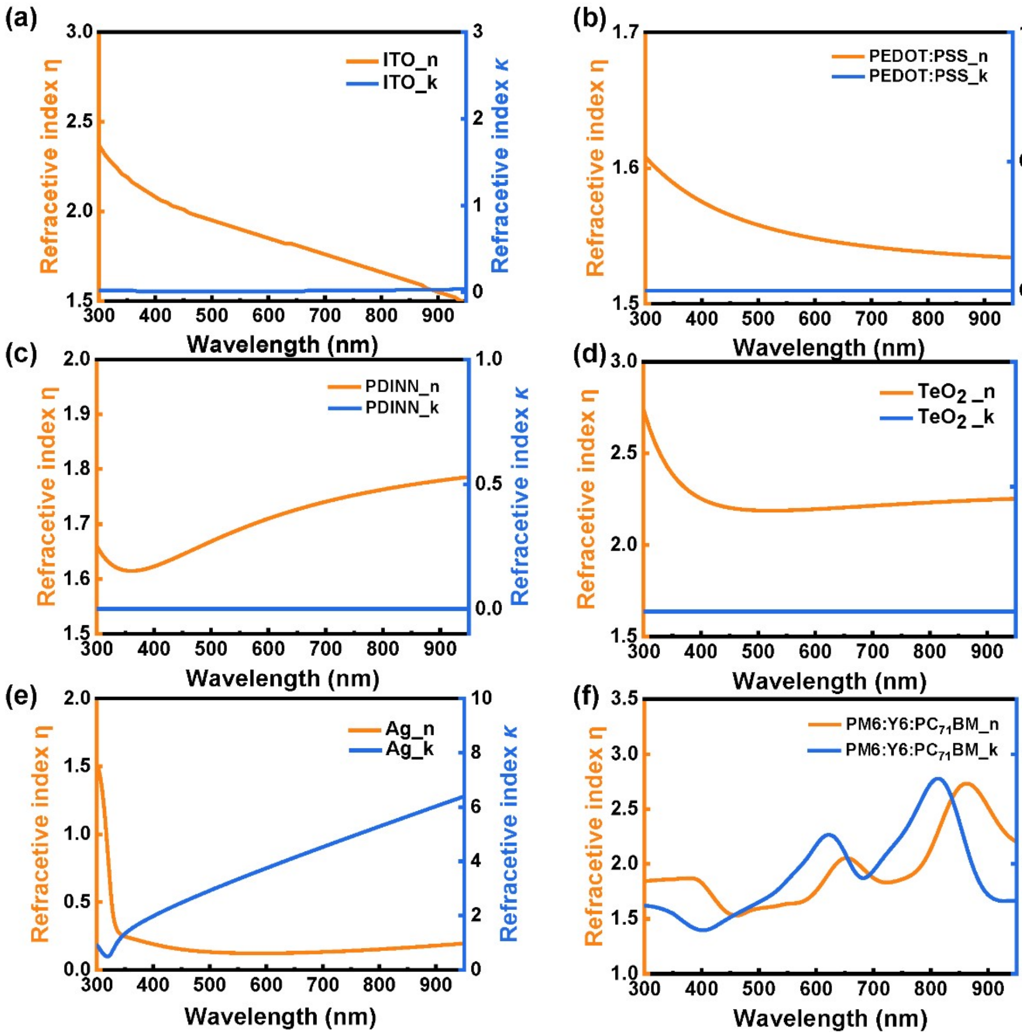

Figure S3. Fitted refractive indexes of different materials. The n (orange lines) and k (blue lines) values of (a) ITO, (b) PEDOT:PSS, (c) PDINN, (d) TeO_2, (e) Ag, and (f) PM6:Y6:$PC_{71}BM$ deposited on silicon wafer.

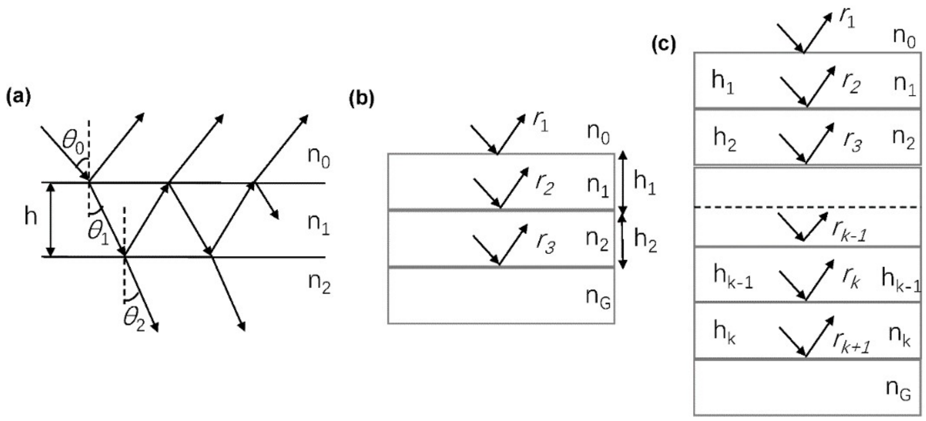

Figure S4. Schematic diagram of antireflective films, (a) single-layer, (b) double-layer, and (c) multi-layer antireflective film.

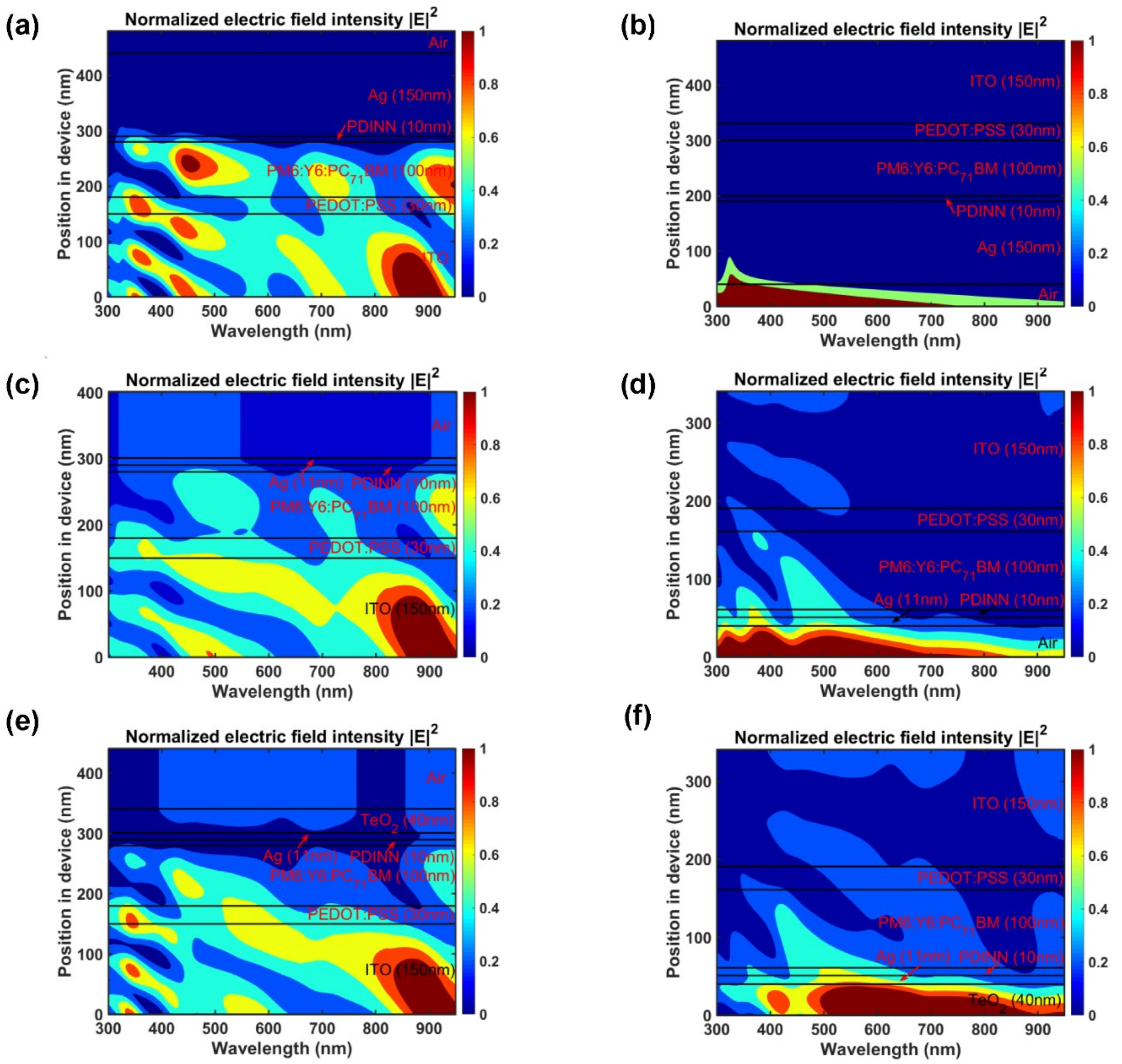

Figure S5. The simulated electric field intensity profiles $|E|^2$ of opaque OPVs with 150-nm Ag electrode from different illumination directions: (a) ITO side and (b) Ag side.The simulated electric field intensity profiles $|E|^2$ of bifacial ST-OPVs with 11-nm Ag electrode from different illumination directions: (c) ITO side and (d) Ag side. The simulated electric field intensity profiles $|E|^2$ of bifacial ST-OPVs with 11-nm Ag electrode and 40-nm TeO_2 from different illumination directions: (e) ITO side and (f) Ag side.

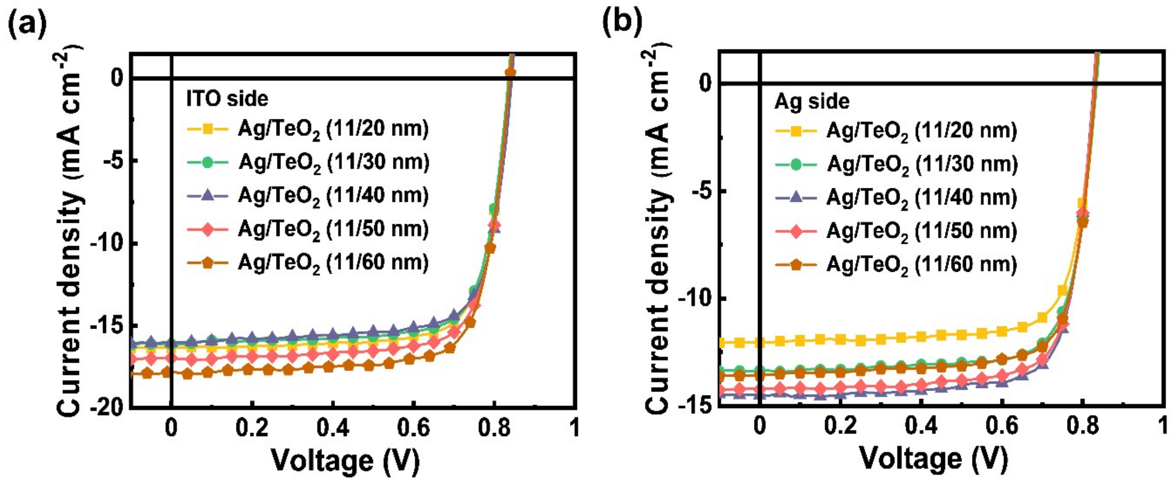

Figure S6. J−V curves of bifacial ST-OPVs with different thickness of TeO_2 layers under the AM 1.5 G (1 sun) illumination through (a) ITO and (b) Ag sides.

Table S1. The photovoltaic performance of the devices based on PM6:Y6 and PM6:Y6:$PC_{71}BM$ blend in this work.

Active layer	J_{SC} (mA cm^{-2})	V_{OC} (V)	FF (%)	PCE (%)	μ_e (cm^2 V^{-1} s^{-1})	μ_h (cm^2 V^{-1} s^{-1})	μ_e/μ_h
PM6:Y6	24.98 (24.80±0.15)	0.859 (0.858±0.001)	75.35 (75.11±0.20)	16.17 （15.98±0.15）	$4.22*10^{-4}$	$1.08*10^{-4}$	3.91
PM6:Y6:$PC_{71}BM$	25.72 (25.67±0.03)	0.874 (0.873±0.002)	76.07 (76.06±0.16)	17.10 (17.04±0.04)	$7.80*10^{-4}$	$6.00*10^{-4}$	1.30

Table S2. Photovoltaic performances of the devices based on PM6:Y6 and PM6:Y6:$PC_{71}BM$ systems.

Active layer	ETL	V_{OC} (V)	PCE (%)	Reference
PM6:Y6	PDINO-G	0.850	16.52	[3]
PM6:Y6	30	0.870	16.28	[4]
PM6:Y6	T2-CNORH	0.863	15.50	[5]
PM6:Y6	ZnO:PBI-SO3H	0.850	15.40	[6]
PM6:Y6	PDIN	0.860	16.17	[7]
PM6:Y6	PNDIT-F3N	0.847	16.76	[8]
PM6:Y6	PDINN	0.847	17.23	[9]
PM6:Y6	PDINN	0.859	16.17	This work
PM6:Y6:$PC_{71}BM$	PDINO	0.861	16.70	[10]
PM6:Y6:$PC_{71}BM$	PDINO	0.850	16.67	[11]
PM6:Y6:$PC_{71}BM$	OSiNDs	0.850	17.15	[12]
PM6:Y6:$PC_{71}BM$	PDINO	0.858	16.40	[13]
PM6:Y6:$PC_{71}BM$	PDINO	0.850	16.75	[14]
PM6:Y6:$PC_{71}BM$	NDI-NI	0.860	16.86	[15]
PM6:Y6:$PC_{71}BM$	TiOxNy	0.850	17.02	[16]
PM6:Y6:$PC_{71}BM$	PDINN	0.874	17.10	This work

Table S3. The photovoltaic and optical parameters of Ag (11 nm)/TeO_2 (20-60 nm) based bifacial ST-OPVs.

Thickness of TeO_2	Illumination	J_{SC} (mA cm^{-2})	V_{OC} (V)	FF (%)	PCE (%)	AVT (%)	Bifaciality factor
20 nm	ITO side	16.35 (16.26±0.07)	0.836 (0.837±0.004)	75.72 (75.44±0.13)	10.35 (10.26±0.06)	26.84	73.53
	Ag side	12.05 (11.94±0.09)	0.830 (0.828±0.004)	76.09 (75.98± 0.14)	7.61 (7.51±0.07)		
30 nm	ITO side	16.13 (15.99±0.10)	0.835 (0.835±0.004)	75.80 (75.37±0.21)	10.21 (10.06±0.12)	27.51	82.76
	Ag side	13.36 (13.23±0.08)	0.834 (0.828±0.004)	75.83 (76.08±0.14)	8.45 (8.33±0.08)		
40 nm	ITO side	16.04 (15.90±0.10)	0.843 (0.836±0.005)	74.99 (75.24±0.14)	10.14 (10.00±0.11)	27.83	90.53
	Ag side	14.51 (14.42±0.08)	0.827 (0.827±0.004)	76.50 (76.31±0.09)	9.18 (9.10±0.07)		
50 nm	ITO side	16.96 (16.71±0.24)	0.838 (0.836±0.005)	75.78 (75.52±0.18)	10.77 (10.54±0.21)	22.93	83.38
	Ag side	14.23 (14.15±0.05)	0.828 (0.827±0.004)	76.22 (76.01±0.13)	8.98 (8.90±0.06)		
60 nm	ITO side	17.82 (17.60±0.21)	0.838 (0.836±0.005)	75.67 (75.47±0.10)	11.30 (11.10±0.17)	21.90	75.84
	Ag side	13.58 (13.51±0.06)	0.832 (0.828±0.004)	75.85 (75.96±0.08)	8.57 (8.49±0.07)		

a) The average values were obtained from over 12 devices.

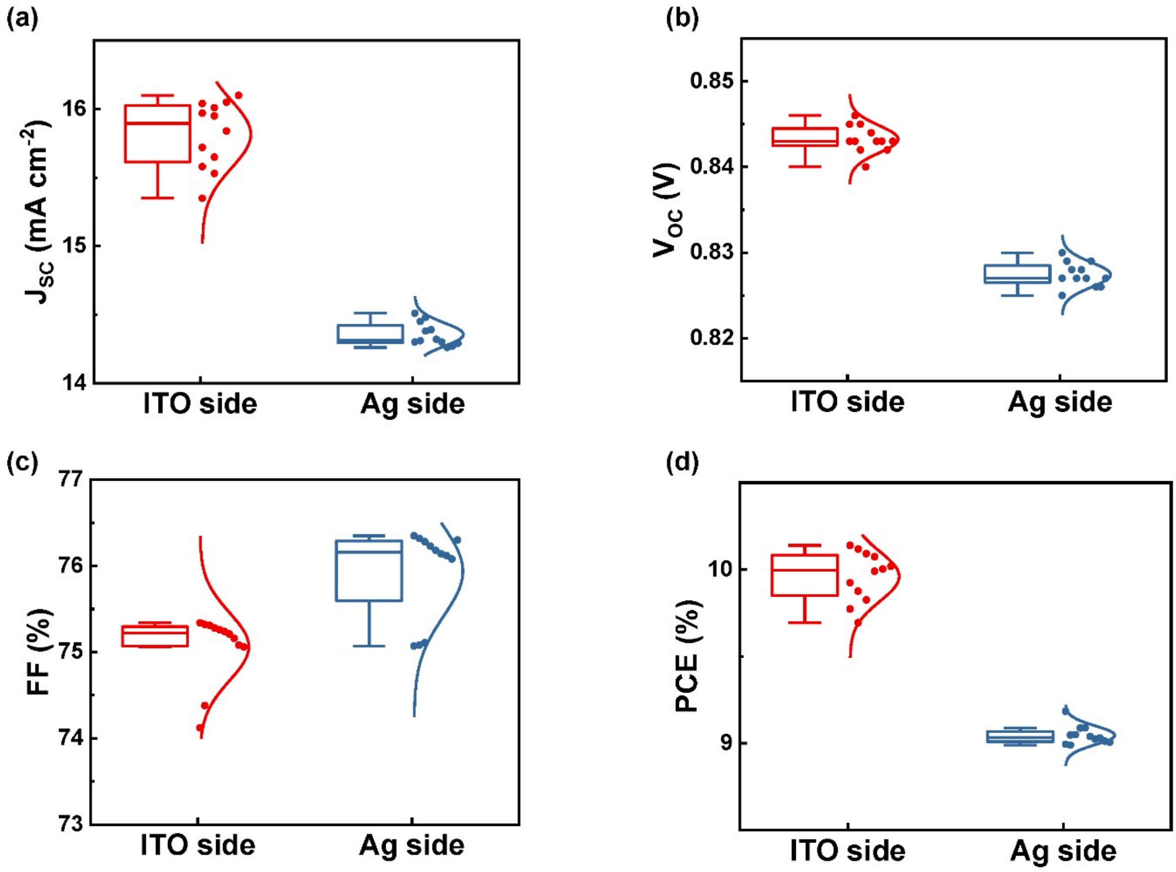

Figure S7. The statistical (a) J_{SC}, (b) V_{OC}, (c) FF, and (d) PCE of Ag/TeO_2 (11/40 nm) based bifacial ST-OPVs under the AM 1.5 G (1 sun) illumination through ITO and Ag sides. The statistical results were obtained from 12 cells.

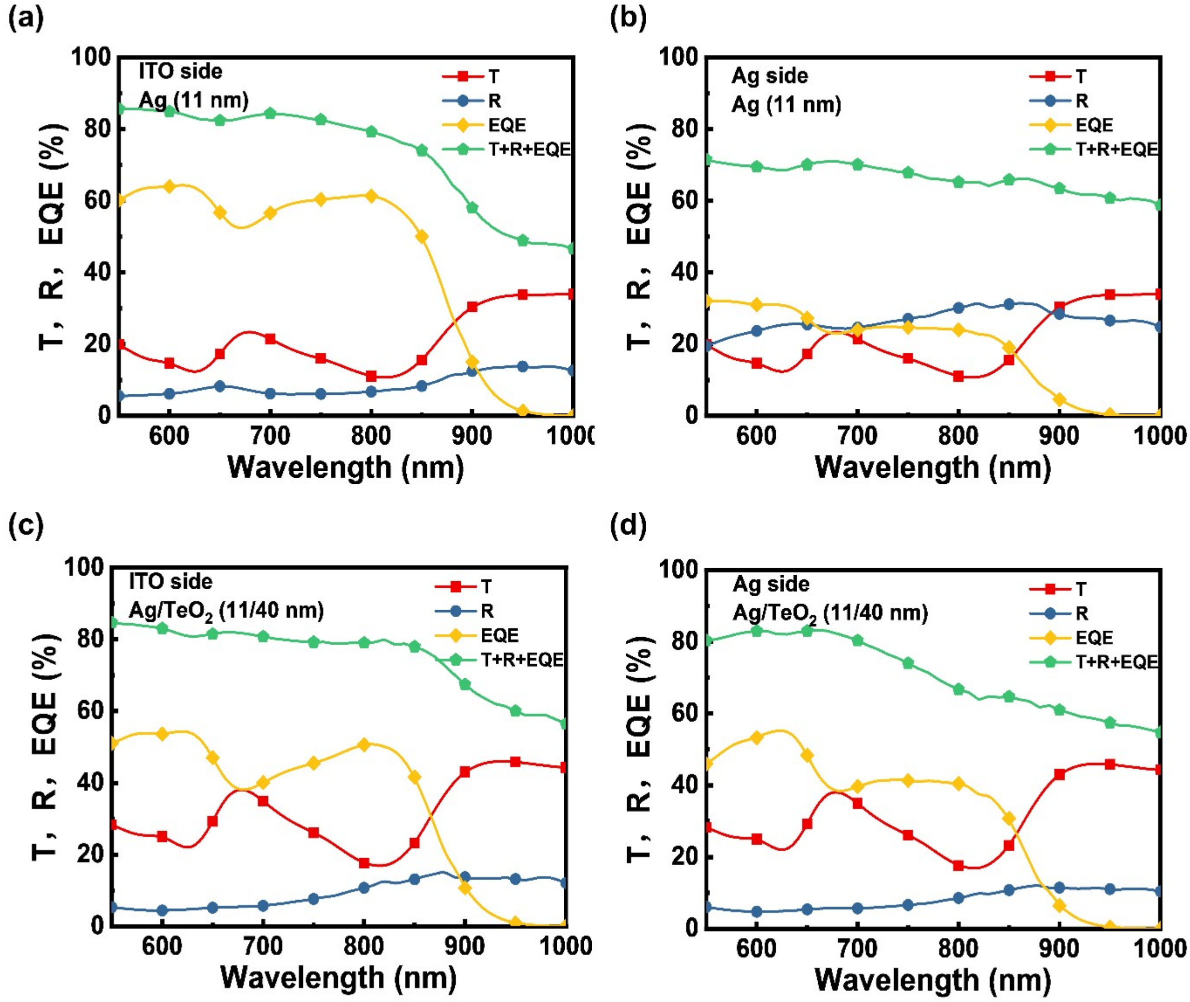

Figure S8. T, R, and EQE curves of bifacial ST-OPVs with or without TeO_2. The data were conducted from the relative devices: bare Ag (11 nm) based ST-OPVs illuminated from (a) ITO and (b) Ag sides, Ag/TeO_2 (11/40 nm) based ST-OPVs illuminated from (c) ITO and (d) Ag sides.

Table S4. The summarized photovoltaic and optical performance of ST-OPVs in this study.

Number	Rear electrode	PCE (%) ITO side/ Ag side	AVT (%)	LUE (%) ITO side/ Ag side	CRI
1	Ag (7 nm)	9.28/6.98	19.70	1.82/1.37	74.55
2	Ag (9 nm)	11.10/6.18	20.21	2.24/1.24	75.09
3	Ag (11 nm)	12.10/5.94	19.20	2.32/1.14	74.56
4	Ag (13 nm)	12.36/4.97	18.82	2.33/0.93	73.08
5	Ag (15 nm)	12.77/4.14	16.25	2.07/0.67	70.22
6	Ag/TeO_2 (11/20 nm)	10.35/7.61	26.84	2.78/2.04	79.51
7	Ag/TeO_2 (11/30 nm)	10.21/8.45	27.51	2.80/2.32	84.37
8	Ag/TeO_2 (11/40 nm)	10.14/9.18	27.83	2.82/2.55	88.28
9	Ag/TeO_2 (11/50 nm)	10.77/8.98	22.93	2.46/2.05	89.07
10	Ag/TeO_2 (11/60 nm)	11.30/8.57	21.90	2.47/1.87	88.20

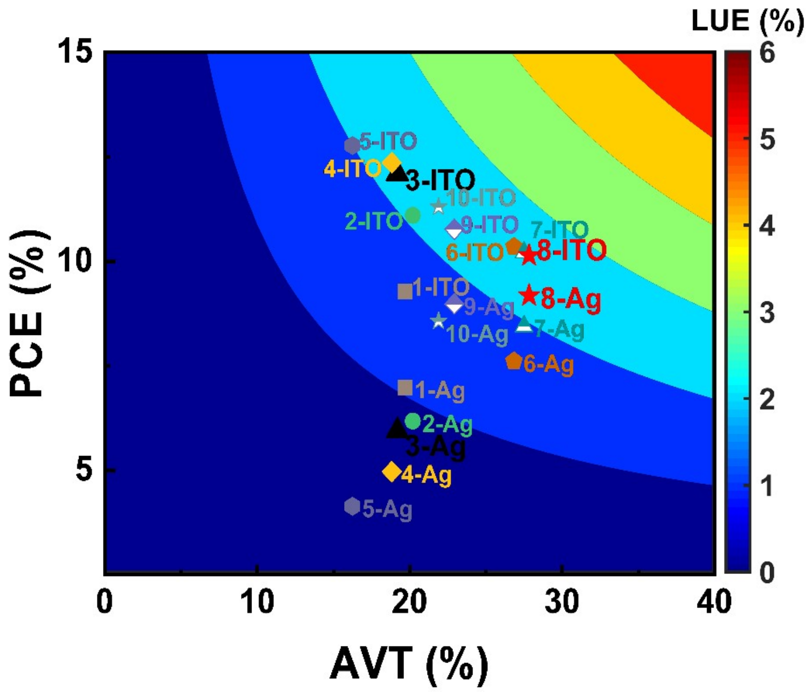

Figure S9. Summarized PCE vs AVT vs LUE plot of ST-OPVs in this study.

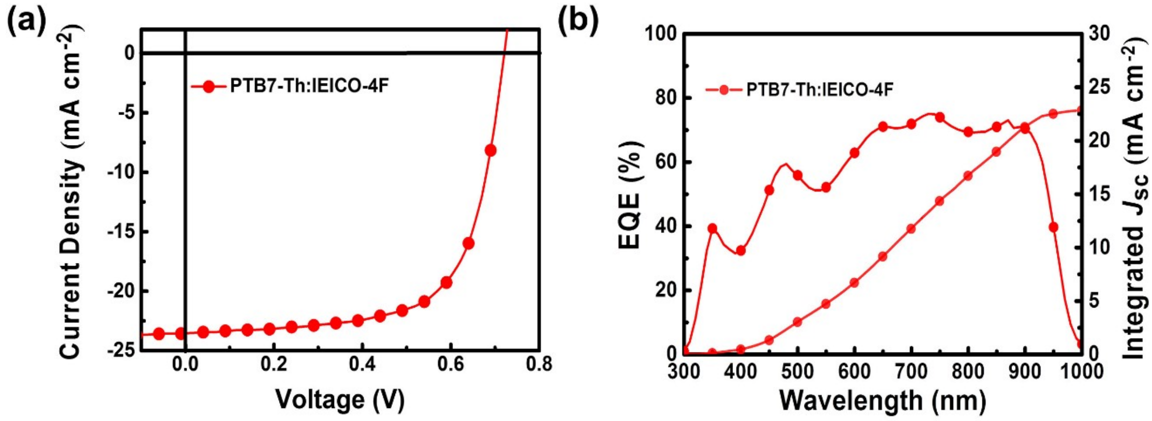

Figure S10. *J-V* curve and EQE spectrum of opaque device using PTB7-Th:IEICO-4F as active layer.

Table S5. The photovoltaic and optical performance of PTB7-Th:IEICO-4F based devices.

Rear electrode	illumination direction	J_{SC} (mA cm^{-2})	V_{OC} (V)	FF (%)	PCE (%)	AVT (%)	LUE (%)	BF	1931 CIE	CRI	CCT
Ag (11 nm)	ITO side	19.05 (18.24)	0.714	66.50	9.05 (9.01±0.02)	33.19	3.00	42.65	(0.271, 0.326)	65.23	9194
	Ag side	8.00 (7.68)	0.691	69.87	3.86 (3.80±0.04)		1.28				
Ag/TeO_2 (11/40 nm)	ITO side	14.60 (14.06)	0.709	66.17	6.85 (6.77±0.07)	46.03	3.15	80.77	(0.292, 0.329)	76.43	7691
	Ag side	11.53 (10.63)	0.693	69.24	5.53 (5.40±0.11)		2.55				
Ag (150 nm)	ITO side	23.53 (22.65)	0.721	67.22	11.40 (11.29±0.09)	-	-	-	-	-	-

The J_{SC} values in brackets were integrated from EQE curves. The average values were obtained from over 6 devices.

References

[1] R. R. Lunt, Theoretical limits for visibly transparent photovoltaics, *Appl. Phys. Lett.*, 2012, **101**, 043902.

[2] C. Yang, D. Liu, M. Bates, M. C. Barr and R. R. Lunt, How to Accurately Report Transparent Solar Cells, *Joule*, 2019, **3**, 1803-1809.

[3] F. Pan, C. Sun, Y. Li, D. Tang, Y. Zou, X. Li, S. Bai, X. Wei, M. Lv, X. Chen and Y. Li, Solution-processable n-doped graphene-containing cathode interfacial materials for high-performance organic solar cells, *Energy Environ. Sci.*, 2019, **12**, 3400-3411.

[4] S. Chen, L. Liu, X. Gao, Y. Hua, L. Peng, Y. Zhang, L. Yang, Y. Tan, F. He and H. Xia, Addition of alkynes and osmium carbynes towards functionalized dpi-ppi conjugated systems, *Nat. Commun.*, 2020, **11**, 4651.

[5] B. Lee, S. Jeong, Y. Cho, M. Jeong, S. M. Lee, J. Oh and C. Yang, Highly Efficient Organic Photovoltaics Enhanced Using Organic Passivation Layer Vacuum Deposition, *Adv. Funct. Mater.*, 2020, **30**, 2005037.

[6] Y. Luo, S. Fang, N. Zheng, L. Liu, F. Würthner and Z. Xie, Increased Electron Transport and Hole Blocking in an Aqueous Solution Processed Dye-Doped ZnO Cathode Interlayer for High Performance Organic Solar Cells, *ACS Appl. Energy Mater.*, 2020, **3**, 1694-1701.

[7] J. Wu, X. Che, H.-C. Hu, H. Xu, B. Li, Y. Liu, J. Li, Y. Ni, X. Zhang and X. Ouyang, Organic solar cells based on cellulose nanopaper from agroforestry residues with an efficiency of over 16% and effectively wide-angle light capturing, *J. Mater. Chem. A*, 2020, **8**, 5442-5448.

[8] T. Yang, R. Ma, H. Cheng, Y. Xiao, Z. Luo, Y. Chen, S. Luo, T. Liu, X. Lu and H. Yan, A compatible polymer acceptor enables efficient and stable organic solar cells as a solid additive, *J. Mater. Chem. A*, 2020, **8**, 17706-17712.

[9] J. Yao, B. Qiu, Z. G. Zhang, L. Xue, R. Wang, C. Zhang, S. Chen, Q. Zhou, C. Sun, C. Yang, M.

Xiao, L. Meng and Y. Li, Cathode engineering with perylene-diimide interlayer enabling over 17% efficiency single-junction organic solar cells, *Nat. Commun.*, 2020, **11**, 2726.

[10] M.-A. Pan, T.-K. Lau, Y. Tang, Y.-C. Wu, T. Liu, K. Li, M.-C. Chen, X. Lu, W. Ma and C. Zhan, 16.7%-efficiency ternary blended organic photovoltaic cells with PCBM as the acceptor additive to increase the open-circuit voltage and phase purity, *J. Mater. Chem. A*, 2019, **7**, 20713-20722.

[11] T. Yan, W. Song, J. Huang, R. Peng, L. Huang and Z. Ge, 16.67% Rigid and 14.06% Flexible Organic Solar Cells Enabled by Ternary Heterojunction Strategy, *Adv. Mater.*, 2019, **31**, 1902210.

[12] M. Cui, D. Li, X. Du, N. Li, Q. Rong, N. Li, L. Shui, G. Zhou, X. Wang, C. J. Brabec and L. Nian, A Cost-Effective, Aqueous-Solution-Processed Cathode Interlayer Based on Organosilica Nanodots for Highly Efficient and Stable Organic Solar Cells, *Adv. Mater.*, 2020, **32**, 2002973.

[13] S. He, Z. Shen, J. Yu, H. Guan, G. Lu, T. Xiao, S. Yang, Y. Zou and L. Bu, Vertical Miscibility of Bulk Heterojunction Films Contributes to High Photovoltaic Performance, *Adv. Mater. Interfaces*, 2020, **7**, 2000577.

[14] Q. Li, Y. Sun, C. Yang, K. Liu, M. R. Islam, L. Li, Z. Wang and S. Qu, Optimizing the component ratio of PEDOT:PSS by water rinse for high efficiency organic solar cells over 16.7%, *Sci. Bull.*, 2020, **65**, 747-752.

[15] M. Liu, P. Fan, Q. Hu, T. P. Russell and Y. Liu, Naphthalene-Diimide-Based Ionenes as Universal Interlayers for Efficient Organic Solar Cells, *Angew. Chem. Int. Ed.*, 2020, **59**, 18131-18135.

[16] X. Yang, Y. Lin, J. Liu, W. Liu, Q. Bi, X. Song, J. Kang, F. Xu, L. Xu, M. N. Hedhili, D. Baran, X. Zhang, T. D. Anthopoulos and S. De Wolf, A Highly Conductive Titanium Oxynitride Electron-Selective Contact for Efficient Photovoltaic Devices, *Adv. Mater.*, 2020, **32**, 2002608.